The International Journal of Advanced Manufacturing Technology (2026) 142:6227–6244
https://doi.org/10.1007/s00170-026-17447-5

ORIGINAL ARTICLE

Assessment of fundamental layer features in monolayer parts fabricated via FFF additive manufacturing under varying printing conditions

Thiago Glissoi Lopes[1] · Giulio Mattera[2] · Paulo Monteiro de Carvalho Monson[1] · Paulo Roberto de Aguiar[3] · Pedro de Oliveira Conceição Junior[1]

Received: 15 August 2025 / Accepted: 5 January 2026 / Published online: 30 January 2026

Abstract

The advancement of Additive Manufacturing (AM) technologies, particularly Fused Filament Fabrication (FFF), has significantly broadened the possibilities for precision manufacturing. However, FFF remains susceptible to geometric distortions that can compromise part quality. This study investigates fundamental layer features in monolayer FFF parts produced under three printing conditions: a standard scenario (H) and two defect induced cases (D1 and D2) introduced via G-code modifications. Using optical microscopy and geometric analysis, we measured region specific features, including contour and raster widths, gap distances, and their variability. Under condition H, contour widths in the right region showed high precision, with mean values of 0.6343 mm (CW1), 0.5886 mm (CW2), and 0.6043 mm (CW3), and standard deviations below 0.07 mm. In contrast, defect condition D1 exhibited reduced uniformity, with CW1 and CW2 decreasing to 0.4647 mm and 0.4402 mm, respectively. In the upper region, D1 led to a pronounced degradation: CW1b decreased to 0.3795 mm and gap dimensions became more variable (e.g., G1b = 0.1884 mm, standard deviation = 0.0346 mm). Under condition D2, the central region exhibited the most severe distortion, with the "d" feature mean reaching 20.17 mm and a standard deviation of 2.41 mm. In addition, monolayer features such as RWA and RWP increased markedly under D2 compared to H, reaching 0.6587 mm and 0.5680 mm, respectively. These findings show that extrusion irregularities can critically affect geometric fidelity. Our results quantitatively link process anomalies to feature deviations in FFF printing, reinforcing the need for improved monitoring and correction mechanisms. Beyond quantifying feature changes under induced defects, this study aims to provide actionable first layer acceptance windows to support in situ monitoring. In practice, the signatures reported here (e.g., raster after width $\geq$ 0.60 mm and inter raster gap $\approx$ 0.35 mm under D2; contour widths $\leq$ 0.50 mm under D1) enable simple camera based screening or ML labeling to (i) flag the defect class in real time and (ii) trigger corrective actions, such as pausing the build or adjusting flow and retraction settings. Future work will explore real time defect detection and adaptive G-code compensation to improve dimensional accuracy and repeatability.

Keywords Fused filament fabrication · Monolayer · Geometric deformation · Fundamental layer features · Optical microscopy

1 Introduction

The Fused Filament Fabrication (FFF) process, also known as Fused Deposition Modeling (FDM), is an additive manufacturing (AM) process that allows the production of three dimensional objects through the additive layering of fused polymer filament according to predetermined infill patterns [1]. These patterns are generated by slicing software, which divides the 3D model into layers of predefined height, generates the toolpaths, and outputs the resulting G-code used

✉ Pedro de Oliveira Conceição Junior
pedro.oliveiracjr@usp.br

[1] Department of Electrical and Computer Engineering - São Carlos School of Engineering, University of São Paulo, São Carlos, Brazil

[2] Department of Chemical, Materials and Industrial Production Engineering, University of Naples Federico II, Naples, Italy

[3] Department of Electrical Engineering, São Paulo State University, Bauru, SP, Brazil

by the Cartesian robot motion platform. The FFF process is distinguished by its high degree of customization; operators can modify infill patterns, densities, and other parameters in the post-processing stage, significantly impacting the final product's quality, production costs, and the prevalence and type of manufacturing defects encountered [2]. The FFF process works by feeding a thermoplastic filament into a heated extruder, softening it and depositing it along a precise path on a heated build platform. This inherently stable, layer-by-layer approach makes FFF machines highly user-friendly and accessible: operators can tweak nozzle and bed temperatures, print speed, layer height, infill density and pattern, and other settings that are often locked down in other AM technologies.

Indeed, process operators have a variety of infill patterns at their disposal, including Grid, Honeycomb, Cubic, Concentric, Rectangular, and Rectilinear, among others [3]. These patterns are subject to modification by several process parameters [4, 5], with infill density or percentage being a particularly influential factor [6]. However, the well-known, user-friendly capabilities of FFF printers do not mean they are immune to errors that can compromise part quality and the integrity of the final components. In the context of AM, the initial layer's fabrication is crucial [7]. A stable first layer generally indicates a successful FFF process, excluding unforeseen disturbances. Inherent process deviations during first layer deposition such as under-extrusion or insufficient bed adhesion can initiate layer misregistration and interfacial delamination that propagate through subsequent layers. Without in situ process monitoring and closed-loop control of key parameters (nozzle temperature, extrusion pressure, and print-head kinematics), geometric fidelity and mechanical integrity deteriorate. This is particularly critical when fabricating complex CAD geometries or deploying advanced infill schemes, which amplify porosity, inter-bead voids, increase surface roughness, dimensional deviations, and compromised structural performance. Therefore, early detection of defects is paramount, especially during the first layer of deposition, allowing for corrective actions or the option to pause printing for operators' assessment, thereby minimizing material waste and associated costs [8, 9].

There is a body of research focused on the production of monolayer parts, workpieces consisting of a single layer, to mimic the first layer's conditions. These studies aim to understand the impact of various process parameters on surface defects, such as in-plane deviation [10] and under-extrusion [11], and other characteristics of the part [10, 12, 13].

Analysis of individual layers within a multi-layered part, or monolayer parts themselves, permits the disaggregation of infill patterns into their constituent printing features. These are commonly categorized as contour and raster printing features [4, 5]. Figure 1 illustrates typical printing features found within a monolayer and is adapted from [14], illustrating the diversity of elements that can be analyzed to improve the FFF process. Quantifying the relationship between process variables and print outcomes not only deepens our understanding of the underlying physico-chemical phenomena, but also enables multi-objective optimization of parameters, whether to minimize part porosity, improve surface finish, or enhance the mechanical performance of the final components.

This work, therefore, asks whether region-specific, first-layer geometry statistics can serve as early, class-specific indicators of under-extrusion (D1) and retraction-seam events (D2). The intended application is twofold: (1) create practical acceptance windows for layer-1 quality control that manufacturers and end-users can apply i immediately,

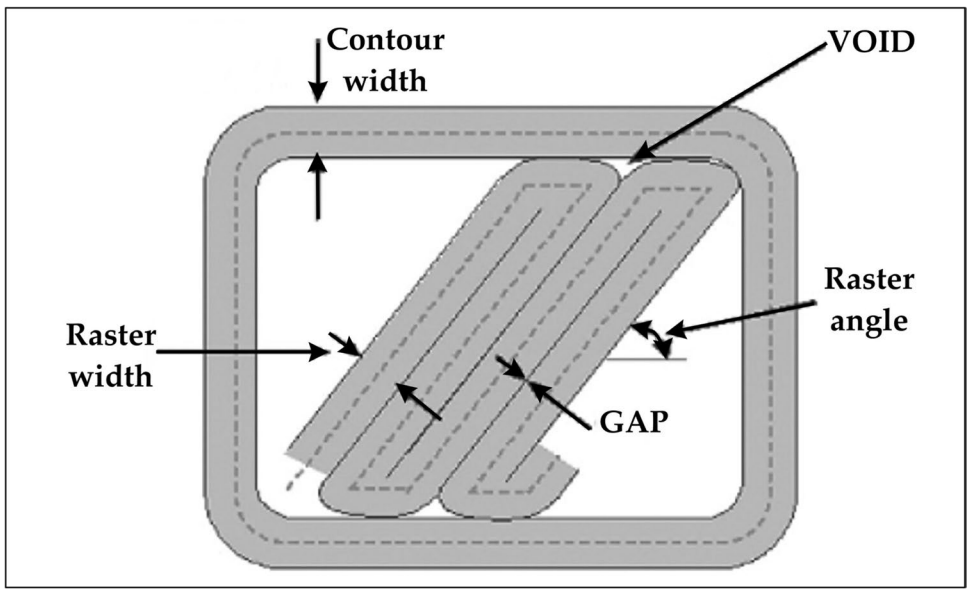

Fig. 1 Monolayer printing features

and (2) generate ground-truth labels and features that could be used in future works to train monitoring modules (from rule-based screening to machine-learning classifiers) that pause the print or adapt flow/retraction parameters when thresholds are exceeded.

2 Assessing FFF parts variability

The variability of parts produced via the FFF process can be explored through a myriad of approaches. Notably, several studies have focused on quantifying the surface and profile roughness of both multilayered and monolayer parts created through FFF [15–17]. Additionally, research has been conducted on identifying defects and geometric anomalies in monolayer FFF parts [18, 19].

The influence of infill patterns on the mechanical properties of both multilayered and monolayer workpieces has also been a subject of investigation [3, 10, 12, 20]. Moreover, the impact of specific monolayer printing features on part properties has been examined. For instance, one study highlighted that an increase in the number of contour lines enhances flexural strength due to a reduction in raster quantity and length, thereby allowing the load to be applied more directly onto the contour lines rather than the raster [21]. Furthermore, the width of the raster has been identified as a crucial factor in determining the build time of a component; the wider the raster, the shorter the build time [5].

The printing sample orientation and raster angle has been shown to significantly affect the mechanical properties of the parts, with different studies illustrating how these factors influence properties such as mechanical strength. For example, [22] demonstrated that the yield strength of ABS printed samples varied from an average of 6.6 MPa for a 45° printing sample orientation to an average of 20.6 MPa for a 0° printing sample orientation, whereas [23] demonstrated that the bending strength of PEEK printed samples varied from 43.2 MPa with the 45°/−45° raster angle to 56.1 MPa with the 0°/90° raster angle.

3 Material and methods

3.1 Monolayer workpiece printing

To investigate the impact of FFF process variations on geometric distortions in single-layer parts, three specific printing scenarios were introduced and fabricated using a A1V2 3D printer by GTMax3D. The A1V2 3D printer is capable of achieving a tolerance of ± 0.05 mm in printed dimensions. For printing the single-layer workpieces, Polylactic Acid (PLA) filament with a 1.75 mm diameter from 3DFila was utilized (Fig. 2).

The initial scenario, designated as regular printing (H), entailed producing a benchmark single-layer rectangular part, colored blue in Fig. 3. The design for this part, with dimensions of 25 × 25 × 0.3 mm, was crafted using the Shapr3D application by Shapr3D Zrt. For this regular scenario, the post-processing was performed using Simplify3D software from Simplify3D LLC, following the default

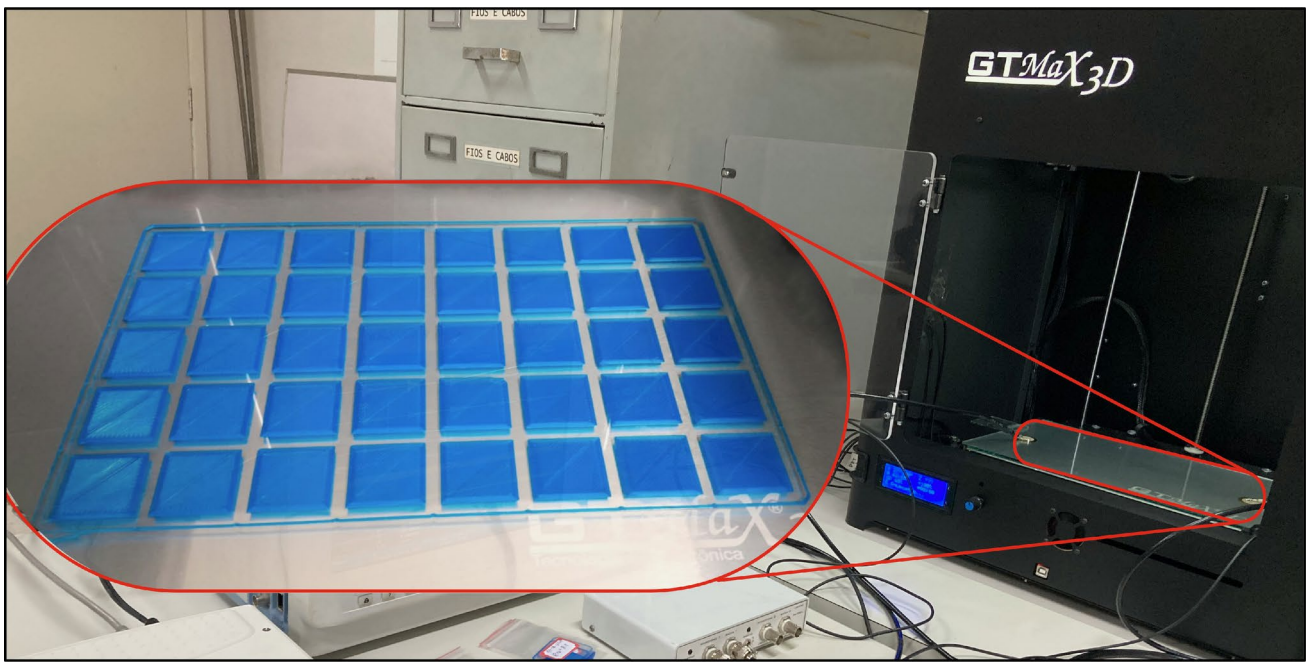

Fig. 2 Printing setup

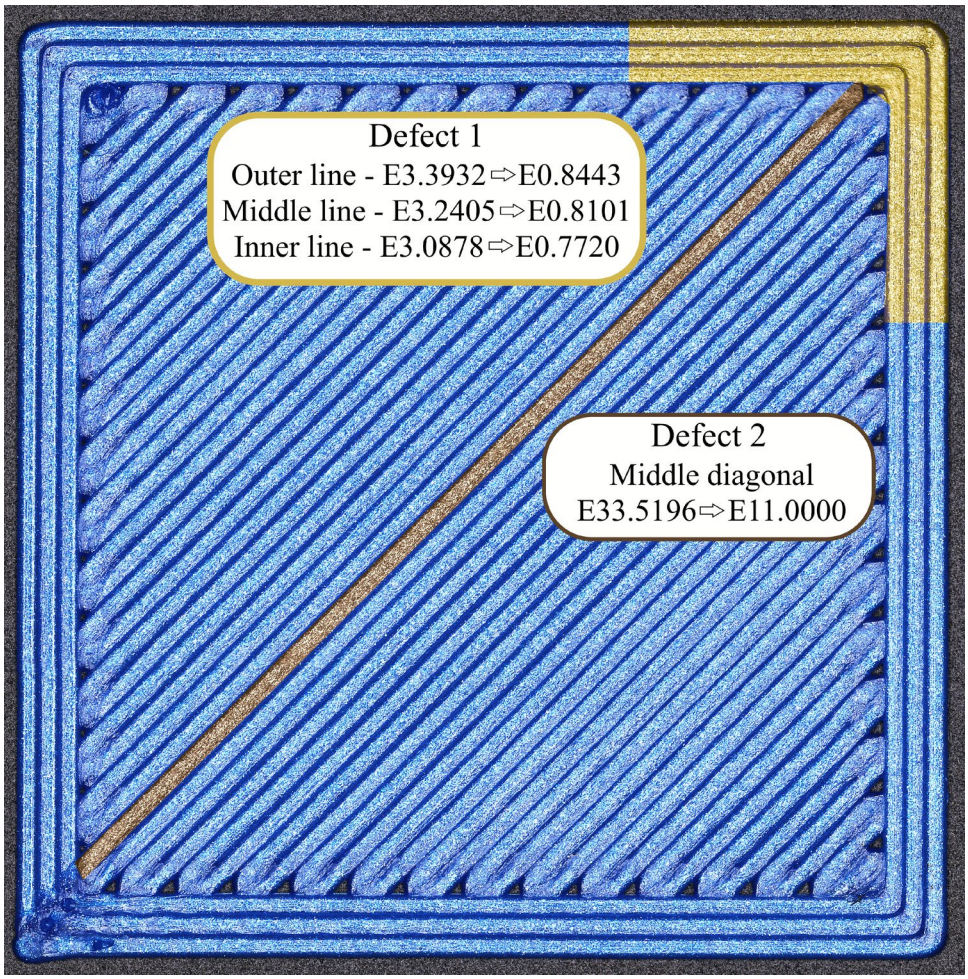

Fig. 3 Printing scenarios sections of interest

post-processing parameter configuration for the A1V2 3D printer by GTMax3D.

The second scenario, named defect 1 (D1), aimed to represent a partially blocked extruder by adjusting the G-code for the regular part, specifically altering the extrusion for three contour lines. This modification involved decreasing the E parameter, which dictates the amount of extrusion in the G-code [24], to approximately 25% of the value for regular printing, categorizing this issue as an irregular polygon defect as classified by [25]. This change was intended to affect the section marked in yellow in Fig. 3.

The final scenario, defect 2 (D2), was produced by editing the G-code segment that draws the central diagonal raster line. We lowered the commanded filament length E below the minimum extrusion threshold, which triggers a brief forced retraction and interrupts material flow, producing a seam defect as classified by [25]. This manipulation mirrors common conditions in which parameters that control retraction and flow are misadjusted while attempting to correct printing issues such as over-extrusion or stringing. Examples include excessive retraction distance or speed, enabling coasting or wiping, setting a negative restart extra distance, overly reducing flow rate, or using a pressure advance that is too high. These settings reduce back pressure and delay material restart, so the line begins underfed and a seam forms. We therefore targeted the central raster line, shown in brown in Fig. 3, to evaluate the direct effect of the defect and its influence on adjacent raster lines. This choice was made to emulate frequent mis-tuning scenarios and to derive actionable, first-layer thresholds for monitoring and feedback control.

The production of parts under each condition was carried out in batches of 40 units, as represented in Fig. 2. The parts produced were also used as foundation for the production of the *MonolayerFFF* image dataset [26, 27]. Following production, 50 workpieces from each printing condition were randomly chosen for microscopic examination.

3.2 Microscopy process

To ensure accurate microscopy procedures, the microscopy test bench displayed in Fig. 4, with labels listed in Table 1, was employed.

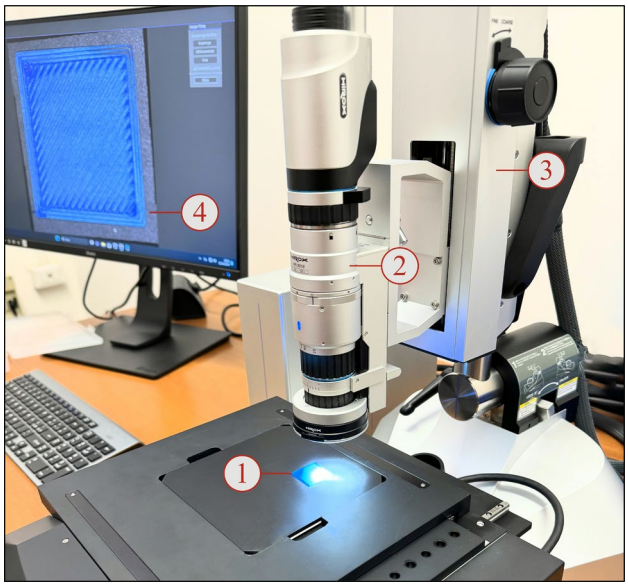

Fig. 4 Microscopy test bench

Table 1 Microscopy test bench labelling

Label	Description
1	Workpiece
2	Hirox HR-2016 Lens
3	Hirox RX-100 (S/N H35438) Microscope
4	HR100 Acquisition software

Table 2 Microscopy test parameters

Condition		D2	D1	H
Magnification		40x	30x	
Acquisition type		Tiling		
Tiling acquisition mode		Multi-focus	2D	
Camera control	Brightness adjustment	AUTO with a value of −16		
	Optimize	ON		

For each workpiece in the 150-part batch, the part was placed on top of the Hirox RX-100 (S/N H35438) microscope bench. The placement location on the microscope bench is represented in Fig. 4 with a label (1). Notably, for all workpieces the same group of Hirox HR-2016 lenses, represented in Fig. 4 with label (2), were employed, as well as the same external light.

Regarding the microscopy test parameters, Table 2 lists the parameters selected for each printing condition evaluation on the HR100 acquisition software. Figure 5 displays an example of the part acquisition configuration on the HR100 software, conducted for the defect 1 (D1) printing condition parts. The test parameters were selected empirically to allow for adequate evaluation of the monolayer printing features and were maintained throughout the microscopic evaluation for each printing condition.

For the D1 and D2 workpiece conditions microscopy, a region-specific acquisition type was conducted, and the images were obtained in.tif format. The region specified was that of the induced defect. That is the upper right corner of the workpiece in the case of the D1, and the middle region of the workpiece in the case of the D2. However, by doing so, in the majority of the workpieces, only a small portion of the defect could be visualized with the specified magnification.

Thus, to achieve a complete representation of the workpiece surface, while also maintaining the same magnification, the Tiling acquisition type was performed for all three printing conditions. In the Tiling acquisition, as represented in Fig. 6, the XY Stage must be defined by a start point and an endpoint. The start point was selected as the upper left corner of the workpiece, and the endpoint was selected as the lower right corner of the workpiece. As a result, multiple images that overlap in boundaries are obtained, and after post-processing, a complete visual representation of the workpiece surface (tiled image) is obtained in.tif format.

For the 2D Tiling acquisition mode, only the start and end points of the XY Stage must be defined. However, for the Multi-focus Tiling acquisition mode, employed in the D2 microscopy, a Z-axis Stage must be defined by a top point and a bottom point. As a result, multiple images that overlap in boundaries and height are obtained, and after postprocessing, a complete visual representation of the workpiece surface with normalized focus of both the workpiece surface and background (tiled image) is obtained in.tif format. The Multi-focus Tiling acquisition mode was selected for the D2 microscopy due to its type of defect which presents a significant background area in the middle region of the workpiece.

3.3 Fundamental layer features evaluation

To enable adequate evaluation of the fundamental layer features of monolayer FFF parts manufactured under different conditions, a variation of the monolayer printing features defined by [14], which are represented in Fig. 1, was evaluated. The monolayer printing features defined by [14] were selected as the foundation for the present study due to variations of these features already being employed in studies for characterizing monolayer FFF parts defects [13, 28].

The part's features evaluation was conducted in the Image Viewer application of the MATLAB R2023b software, from MathWorks. The obtained values, in pixels, were exported to the MATLAB workspace as vectors. After being exported to the workspace, the values were converted from pixels to mm by employing the known length of the workpiece as a reference. Following this, the mm values were saved in

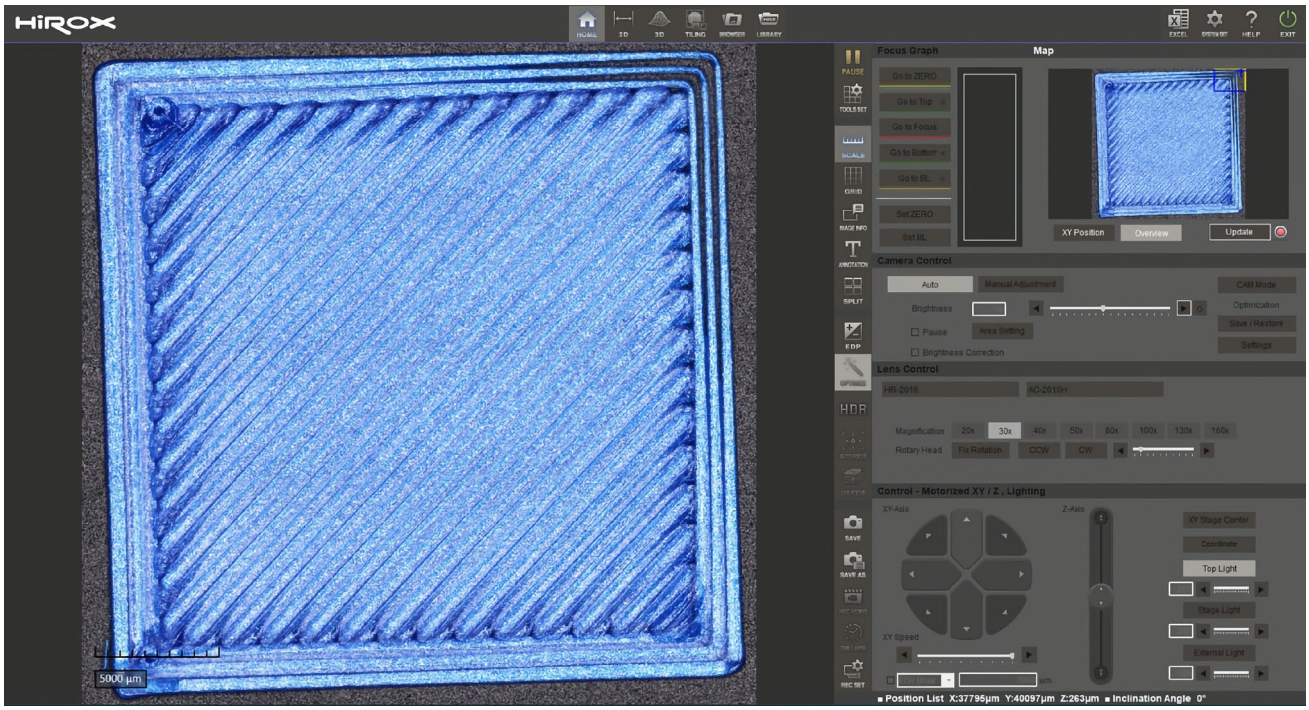

Fig. 5 Part acquisition configuration

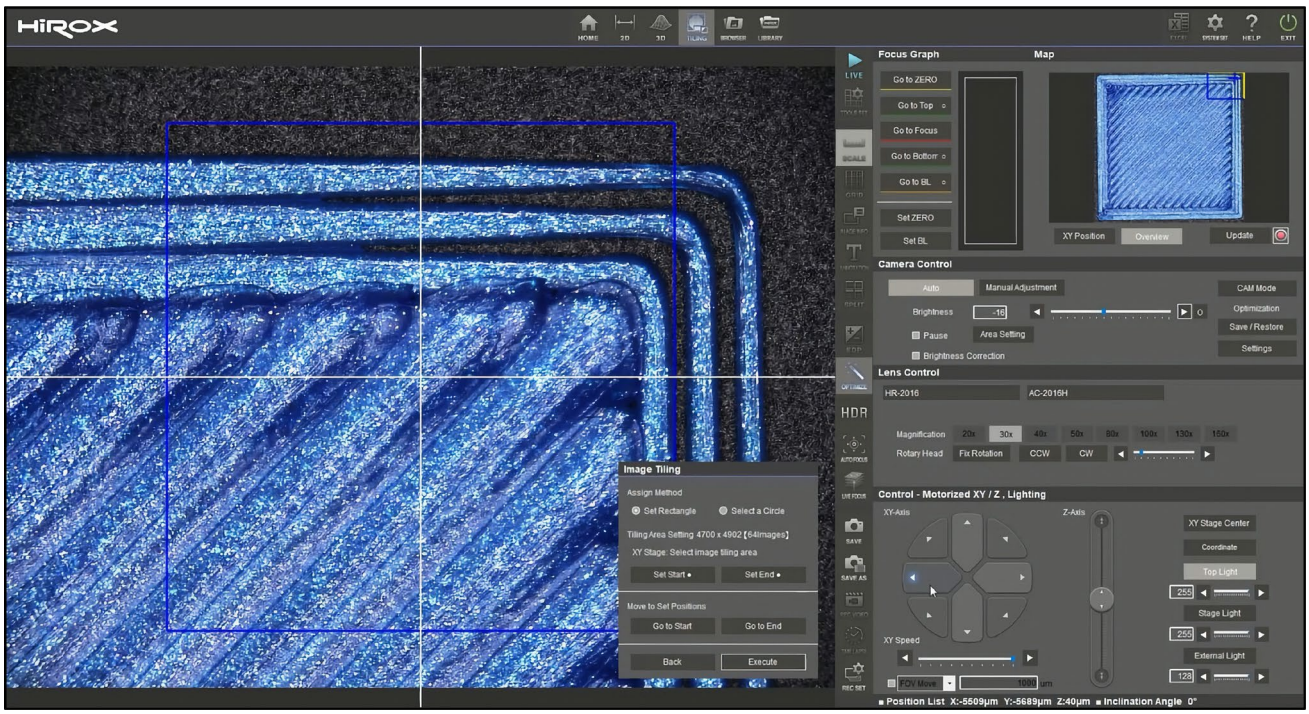

Fig. 6 Tiling example

the MATLAB workspace as matrices, which allowed for the statistical analysis detailed subsequently.

The evaluation of the monolayer printing features of H printed parts was divided into three distinct phases: an assessment of the right side of the H workpiece; An examination of the upper side of the H workpiece; and an examination of the center region of the H workpiece. Both the right side and upper side analyses of the H workpiece it involved the measurement of each contour line's width (CW1, CW2, CW3), as can be observed in Fig. 7. In contrast, the center

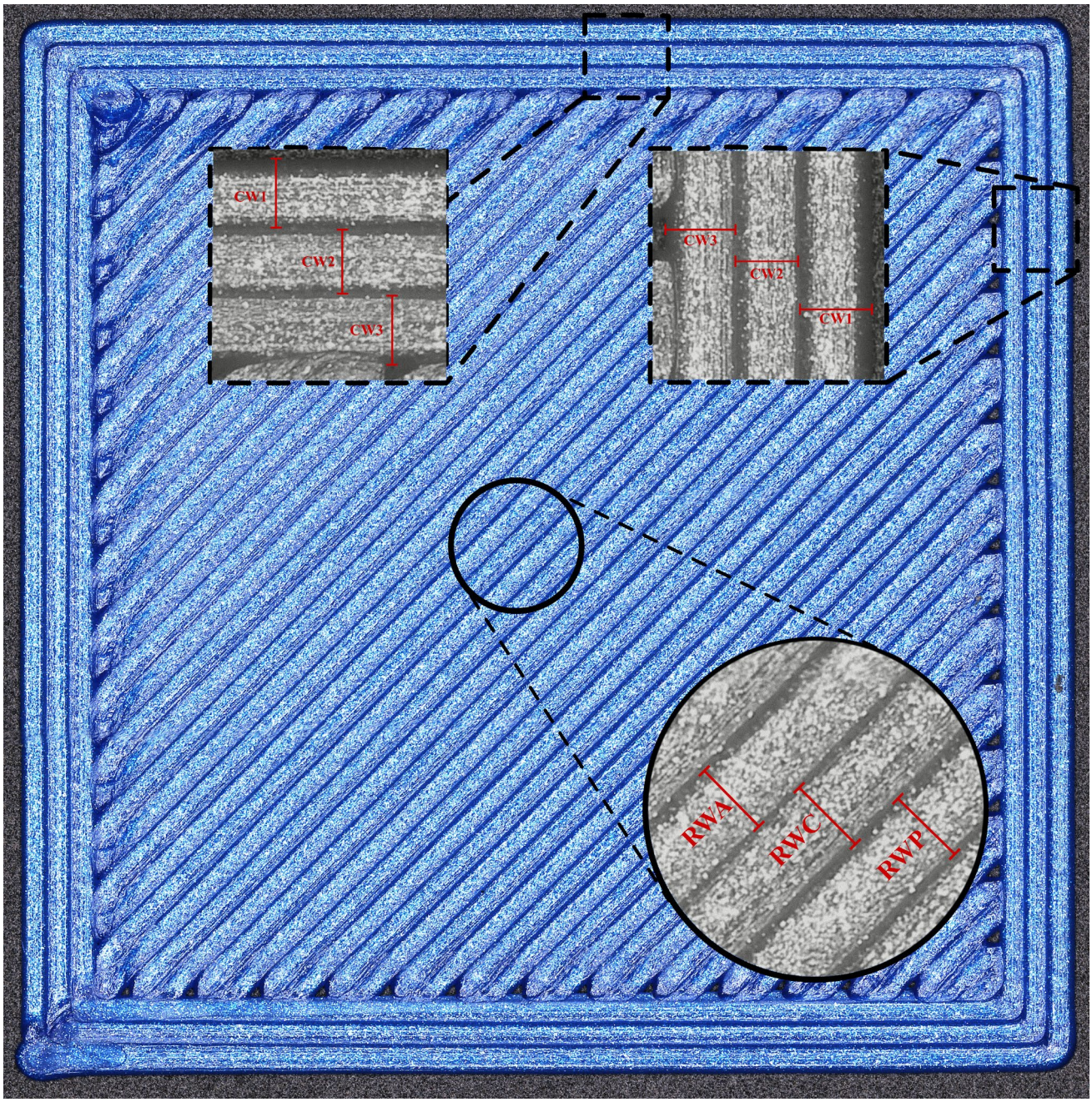

Fig. 7 H monolayer features

area analysis focused on evaluating three raster line widths: RWP, which is the raster line previous to the center one; RWC, which is the center raster line; RWA, which is the raster line after the center one.

The evaluation of the monolayer printing features of parts affected by the D1 defect was divided into two distinct phases: an assessment of the right side of the D1 workpiece, focusing on the initial manifestation of the defect, and an examination of the upper side of the D1 workpiece, concentrating on the defect's conclusion. The analysis of the right side, as detailed in Fig. 8, involved the measurement of each contour line's width (CW1, CW2, CW3), along with the gap between these lines (G1 between CW1 and CW2, and G2 between CW2 and CW3). Additionally, a novel parameter "d" was introduced to quantify the length variation between the onset points of the D1 defect within the gaps G1 and G2.

In contrast, the analysis of the upper side of the D1 parts, as presented in Fig. 9, entailed a measurement of each contour line's width at two distinct points within the measurement area (CW1, CW2, CW3). This approach was

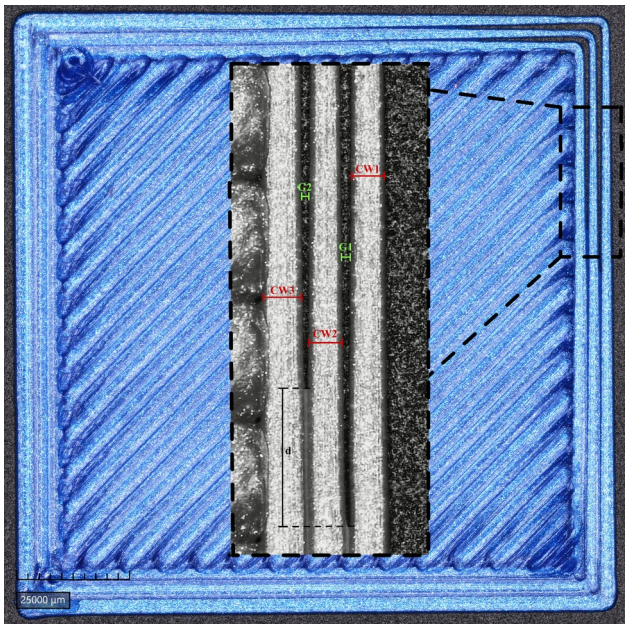

Fig. 8 D1 monolayer features the right side

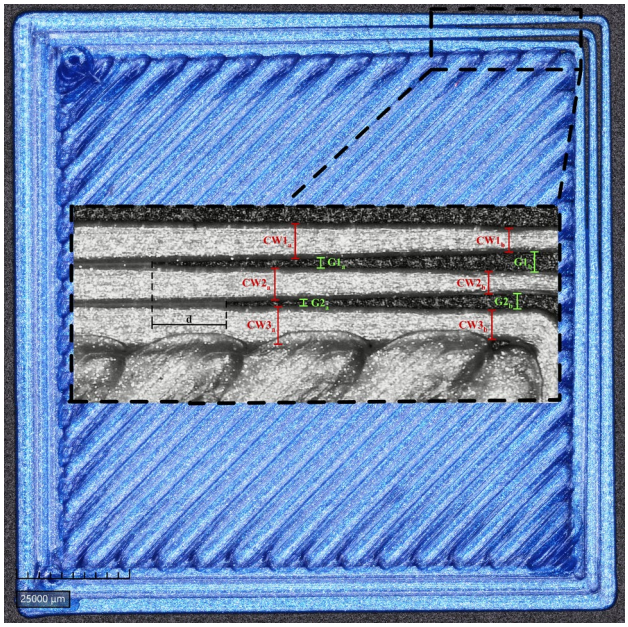

Fig. 9 D1 monolayer features an upper side

necessitated by the noticeable variance in contour widths on the upper side of the D1 parts. Consequently, two sets of values were derived for each contour line's width ($CW1_a$, $CW1_b$; $CW2_a$, $CW2_b$; $CW3_a$, $CW3_b$). Similarly, the gap between these lines was measured at both points, resulting in values $G1_a$ (between $CW1_a$ and $CW2_a$), $G2_a$ (between $CW2_a$ and $CW3_a$), $G1_b$ (between $CW1_b$ and $CW2_b$), and $G2_b$ (between $CW2_b$ and $CW3_b$). Furthermore, the parameter "d" was also assessed on the upper side of the D1 parts,

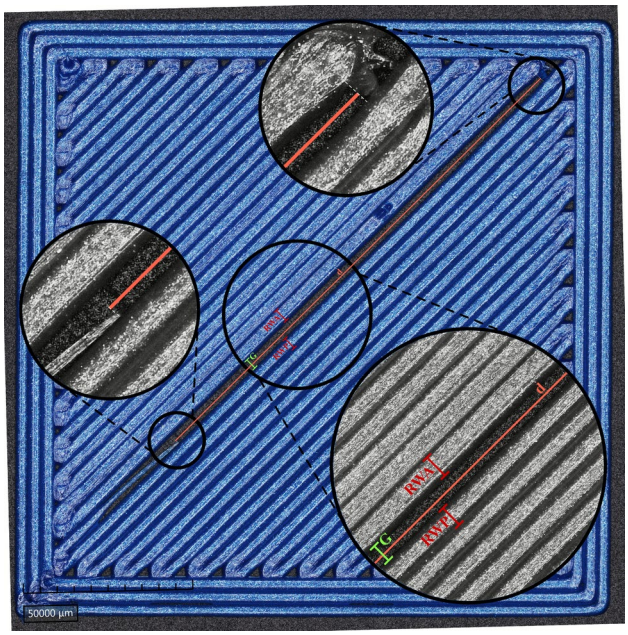

Fig. 10 D2 monolayer features

quantifying the length variation between the onset points of the D1 defect within the gaps G1 and G2.

The analysis of monolayer printing features in parts influenced by the D2 defect was segmented into three phases: first, an evaluation of the middle section of the D2 workpiece to assess the defect's impact on the raster lines; second, a focused inspection of the lower left corner of the internal workpiece area, to identify the onset of the defect; and third, an analysis of the upper right corner of the internal workpiece area to observe the defect's termination.

As depicted in Fig. 10, these phases entailed measurements of raster width before the gap (RWP), raster width after the gap (RWA), and the intervening gap (G). Furthermore, the introduction of the parameter "d" enabled the measurement of the length spanning from the beginning to the end of the D2-impacted region.

Initially, the repeatability of the printing process was assessed by examining the distribution of mean width and standard deviation (std) values for the contour, raster, and gap features across workpieces, calculated using MATLAB's "mean" and "std" functions. The distributions of these mean and std values were analyzed via histogram plots in MATLAB, with default histogram attributes. The distributions represented in the histograms were compiled in four figures:

1. Mean width between contours or rasters of each workpiece;
2. Std width between contours or rasters of each workpiece;
3. The mean gap between contours or rasters of each workpiece;

4. The std gap between contours of each workpiece.

Following this, the study aims to evaluate the impact of defects on the workpieces by comparing the mean and std values of each printing feature across defective and regular workpieces. It is critical to note the specific nature of the "d" printing feature/parameter in the D1 and D2 conditions and the "G" printing feature in the D2 condition, which only presents a single value per workpiece, limiting the analysis to comparative evaluations.

4 Results and discussion

4.1 Repeatability analysis

4.1.1 Regular condition (H)

In the analysis of the mean width distributions under the regular (H) condition, depicted in red in Fig. 11, a clear distinction is observed between the behaviors of the contour lines of both the right and upper regions and the raster lines in the central region. The contour lines, both H right and H upper, demonstrate a more compact distribution pattern, while the raster lines (H center) exhibit a wider spread. Notably, for the H center distribution, the mean width values for 6 out of 50 workpieces, equivalent to 12%, fall within the range of 0.35 mm to 0.40 mm.

Further examination of the mean width distributions under the regular (H) condition in the upper, right, and center regions also sheds light on the average width derived from these distributions. Considering the A1V2 printer's tolerance of ± 0.05 mm, it is found that the contour width spans predominantly between 0.55 mm and 0.65 mm for 96% of the workpieces, leading to the establishment of an average contour line width at 0.60 mm ± 0.05 mm for the H condition. In contrast, the raster width, for the majority of parts, 82%, ranges between 0.50 mm and 0.60 mm, allowing the determination of an average raster line width at 0.55 mm ± 0.05 mm for the H condition.

These findings underscore the precision inherent in the H condition's printing characteristics of both contour and raster lines, with a majority of parts falling within the stipulated printer tolerance of ± 0.05 mm. However, a slight deviation in precision is observed between the raster and contour dimensions, where the raster's adherence to the tolerance

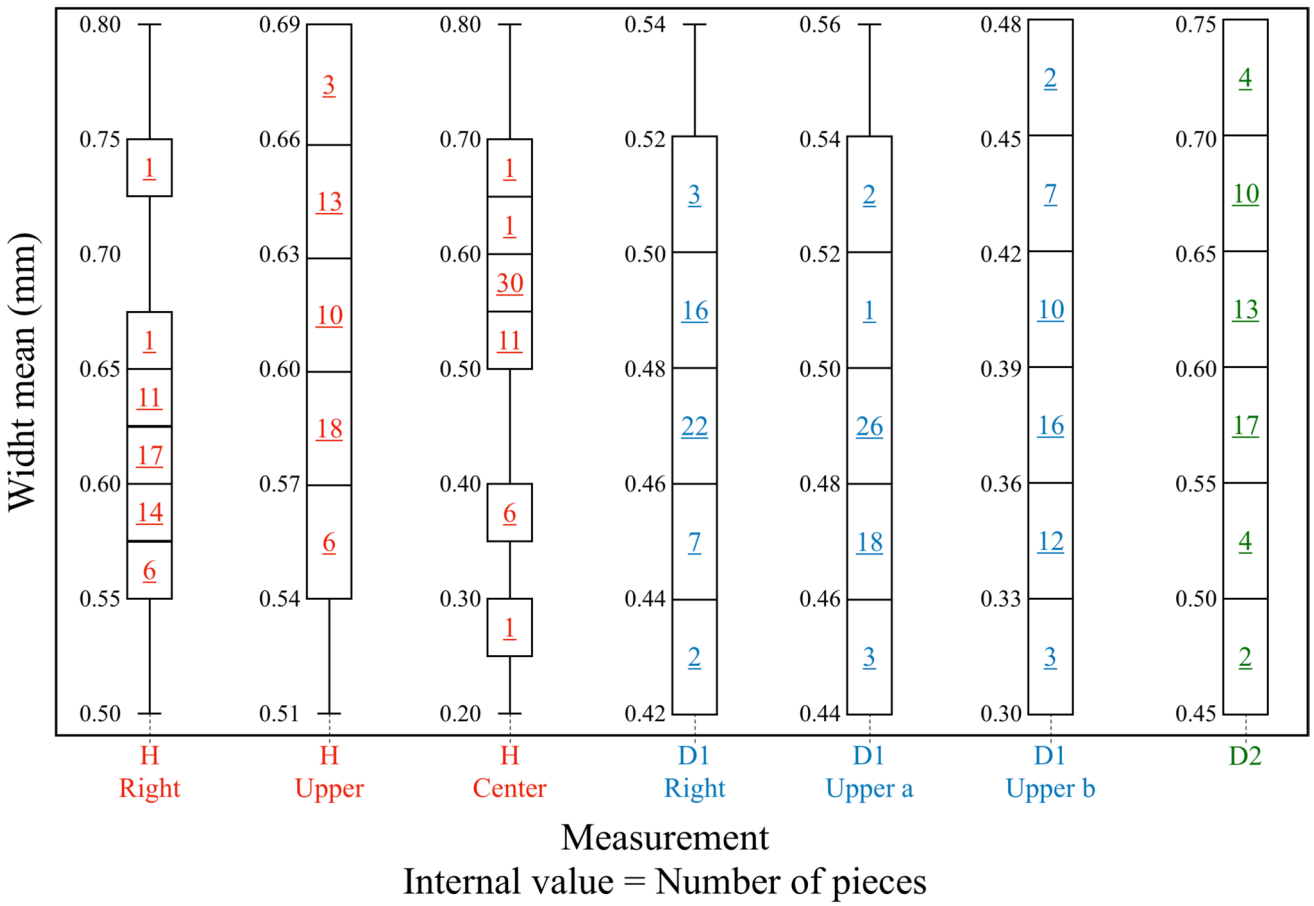

Fig. 11 Mean width between contours or rasters of each piece

range is slightly lower at 82% compared to the contour's 96%.

In the analysis of standard deviation (std) width distributions under the regular (H) condition, represented in red in Fig. 12, distinct behaviors emerge between the regions when considered within the printer's tolerance range of ± 0.05 mm. Specifically, for the contour lines in both the H Right and H Upper regions, it is noted that 76% of the parts exhibit a width std of less than 0.05 mm. Conversely, within the H Center region's raster lines, a higher proportion, 94% of the parts, demonstrate a width std of less than 0.05 mm. This discrepancy highlights a greater uniformity in the width values of raster lines compared to contour lines in the H printing condition.

4.1.2 Defect 1 condition (D1)

In the analysis of the mean width distributions under the defect 1 (D1) condition, depicted in blue in Fig. 11, a clear distinction is observed between the behaviors of the contour lines of the evaluated right and upper regions. Comparatively, concerning the distribution patterns, both "Right" and "Upper a" mean width values fall within the stipulated printer tolerance of ± 0.05 mm. With the average contour line width at 0.47 mm ± 0.05 mm for the "Right" side, and an average contour line width at 0.49 mm ± 0.05 mm for the "Upper a" side.

Thus, it is possible to observe that even with the width shrinkage caused by the D1 defect, the contour lines fabrication repeatability is high, with 100% of the values for both "Right" and "Upper a" regions, and 90% of the values for the "Upper b" region falling within the printer tolerance of ± 0.05 mm. The "Upper b" region presents a slightly lower contour width mean of 0.39 mm ± 0.05 mm in 90% of the cases.

In analyzing the standard deviation (std) width distributions associated with defect 1 (D1), depicted in blue in Fig. 12, it was observed that 86% of the parts in both the D1 Right and D1 "Upper b" regions fall within the printer's tolerance range of ± 0.05 mm, exhibiting a width std of less than 0.05 mm. Notably, the D1 "Upper a" region demonstrated even greater uniformity, with 96% of parts presenting a width std of less than 0.05 mm. These findings suggest that despite the shrinkage in contour line width attributed to the D1 defect, it does not lead to reduced uniformity among contour lines within a workpiece. Therefore, it can

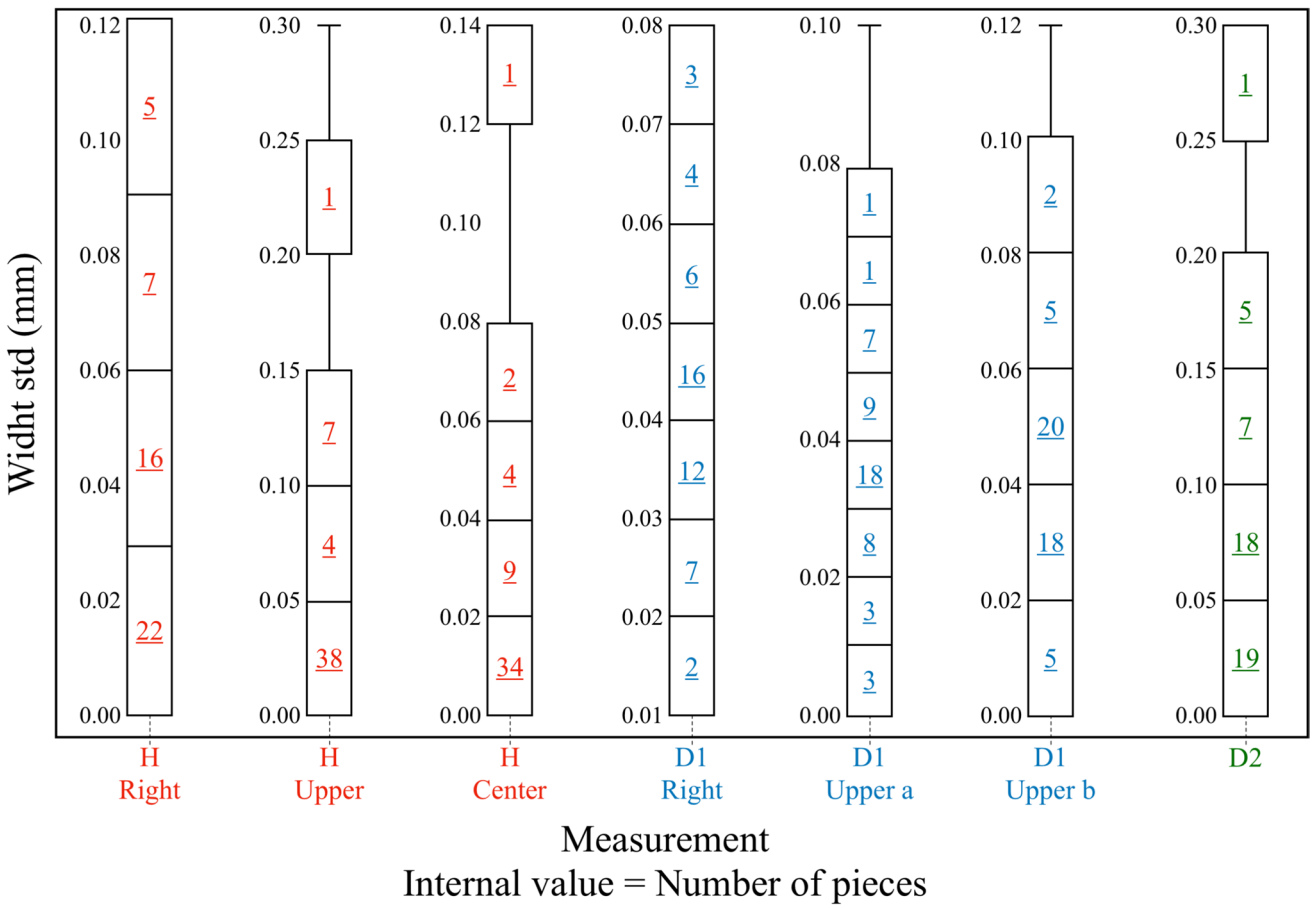

Fig. 12 Std width between contours or rasters of each piece

be inferred that the presence of the defect in the contour printing monolayer feature does not necessarily result in increased variability in the printing process.

4.1.3 Defect 2 condition (D2)

In the analysis of the mean width distributions under the Defect 2 (D2) condition, which is illustrated in green in Fig. 11, a distinction is noticeable in the behavior of the raster lines relative to the H Center. Specifically, concerning the distribution patterns, 80% of the raster-line workpieces under the D2 condition fall within the printer's tolerance range of ± 0.05 mm, exhibiting an average width of approximately 0.65 mm ± 0.05 mm. This comparison reveals that the distribution patterns of both D2 and H center raster lines are similarly aligned, with 80% of D2 and 82% of H center lines adhering to the printer's tolerance specifications. However, a subtle difference is evident in the average raster width, recorded at 0.65 mm ± 0.05 mm for D2 and 0.55 mm ± 0.05 mm for the H center.

The std results under the Defect 2 (D2) condition, illustrated in green in Fig. 12, reveal a different scenario. It is observed that only 38% of the workpieces remain within the printer's tolerance range of ± 0.05 mm, with a width standard deviation (std) of less than 0.05 mm. This starkly contrasts the outcomes observed for the D1 condition. These findings suggest that the D2 defect mechanism and its specific characteristics considerably disrupt the uniformity of the raster lines' fabrication, leading to a notable disparity in width among the lines. This effect underscores the significant impact of the D2 defect on the consistency of the printing process.

4.1.4 GAP monolayer feature

The analysis of the GAP monolayer feature focuses on the average gap sizes (Gap mean) within different regions under the D1 condition, namely, the Right and Upper areas are represented in blue in Fig. 13. The analysis reveals significant variations in gap length across these regions, with notable differences, particularly in the Upper areas.

In the D1 Right and D1 "Upper a" regions, all workpieces were found to have gap sizes within the printer's tolerance range of ± 0.05 mm. Specifically, the average gap size is 0.11 mm ± 0.05 mm for the D1 Right and 0.10 mm ± 0.05 mm for the D1 "Upper a" regions. This consistency underscores a high level of repeatability in the printing process, even when the observed monolayer feature appears as the result of the occurrence of a defect in the contour lines printing.

Upon examining the D1 "Upper b" region, it was observed that 90% of the workpieces still fall within the printer's tolerance range, with an average gap size of 0.18 mm ± 0.05 mm. This adherence rate, although slightly lower than in other regions, remains impressively high. It reflects the printing process's overall robustness, showcasing its ability to maintain a high standard of quality and precision across different sections of the printed workpieces, even in the presence of minor inconsistencies.

The analysis of the GAP lengths generated by the D2 defect, specifically between the raster lines and highlighted in green in Fig. 13, shows a wider distribution compared to previous findings, with the Gap mean ranging from 0.10 mm to 0.50 mm. This significant deviation suggests that the mechanism underlying the D2 defect impacts the appearance of the GAP monolayer feature in a markedly different manner than the D1 defect does.

The analysis of Gap standard deviation (std) distributions for workpieces affected by defect 1 (D1), illustrated in blue in Fig. 14, reveals a high level of uniformity within the printer's tolerance range of ± 0.05 mm. Specifically, 96% of workpieces from the D1 Right region, 100% from the D1 "Upper a" region, and 98% from the D1 "Upper b" region exhibited a gap size standard deviation lower than 0.05 mm. This consistency suggests that the shrinkage in contour line width caused by the D1 defect does not compromise the uniformity of GAP lengths across a given workpiece.

4.2 Comparisons analysis

To evaluate the impact of the defects on the workpieces, a comparison was made between the mean and standard deviation values of each monolayer printing feature across defective and regular workpieces, separating the analysis into three regions of the workpieces: Right, Upper, and Center.

A first analysis of the Right region results, represented in Table 3, reveals insights into monolayer features under two distinct conditions, H and D1, assessed through measurements of contour widths (CW1, CW2, CW3) and gaps (G1, G2) lengths on batches of 50 workpieces for each condition. Under condition H, mean widths spanned from 0.5886 mm to 0.6343 mm, with standard deviations (Std) ranging from 0.0361 mm to 0.0678 mm. These Std values, particularly for CW2 and CW3, fall within the printer's tolerance range of ± 0.05 mm, indicating exceptional measurement precision and consistency in monolayer widths.

For condition D1, a differentiation in monolayer features was observed, notably with reduced mean widths for CW configurations, exemplified by CW1 at 0.4647 mm, suggesting a pronounced impact of the D1 defect on monolayer formation. The introduction of gap measurements under D1, G1 between CW1 and CW2, and G2 between CW2 and CW3, further elucidates the D1 defect effect, with mean values for G1 and G2 at 0.1117 mm and 0.0958 mm,

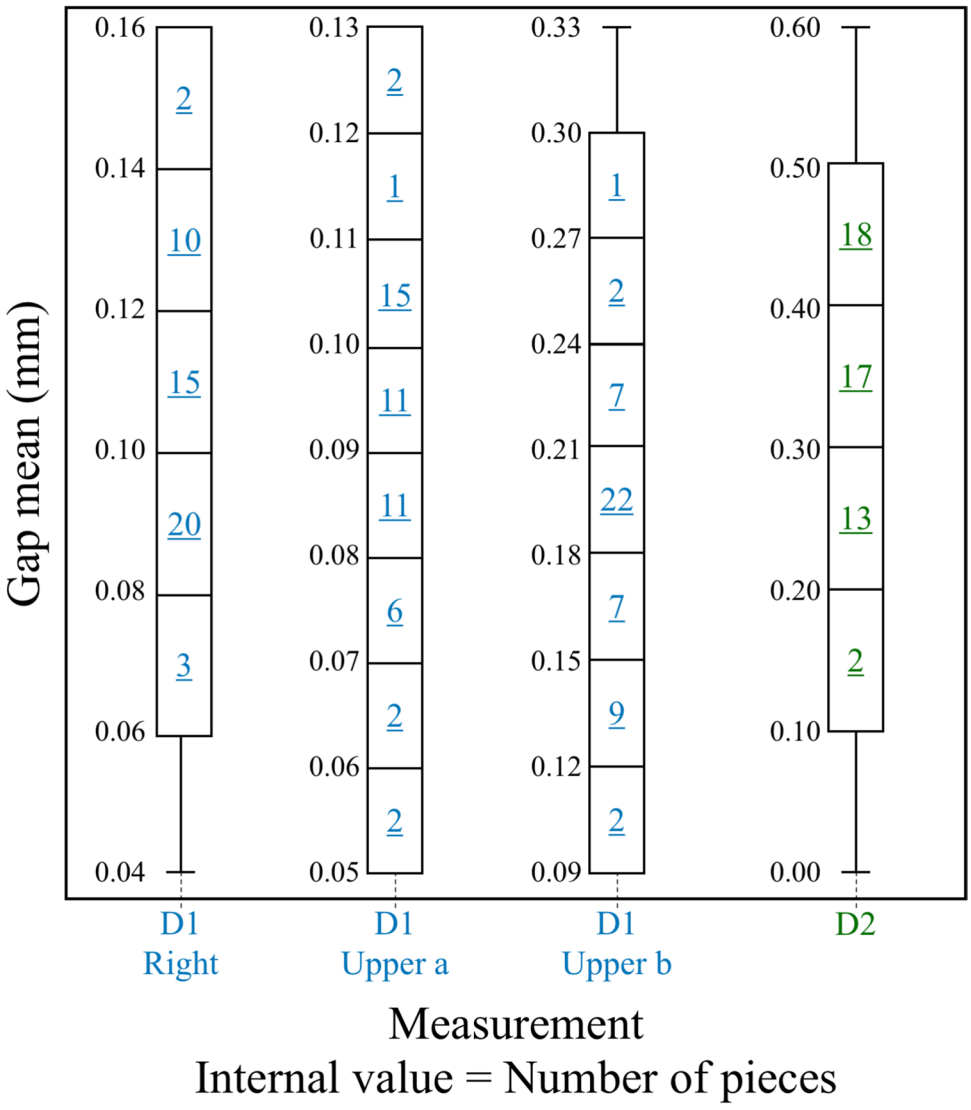

Fig. 13 The mean gap between the contours or rasters of each piece

respectively. These values are significantly lower than those for CW measurements, underscoring a marked distinction in feature size under D1 conditions, likely reflective of specific material behaviors or process influences on monolayer characteristics.

Moreover, the standard deviations for CW2 under condition D1 and for both gap configurations (0.0203 mm, 0.0162 mm, and 0.0265 mm, respectively) fall below the printer's tolerance threshold, signifying that these measurements not only highlight a variance in monolayer characteristics under different operational scenarios but also confirm the high precision of these measurements within the defined tolerance range.

A first analysis of the Upper region results, represented in Table 4, reveals insights into monolayer features under two distinct conditions, H and the sub-regions "a" and "b" of the Defect 1 (D1) condition, assessed through measurements of contour widths (CW1, CW2, CW3) and gaps (G1, G2) lengths on batches of 50 workpieces for each condition.

For condition H, mean widths are observed ranging from 0.5890 mm to 0.6474 mm, with the standard deviations indicating the precision of these measurements. The standard deviation values for CW2 and CW3 fall within the printer's tolerance range of ± 0.05 mm, denoting high precision. Conversely, CW1's higher standard deviation of 0.0784 mm suggests more variability under this condition.

Under the D1 condition, divided into sub-regions "a" and "b", we see a delineation in monolayer features. In sub-region D1a, mean widths show a reduction when compared to condition H, with CW1a at 0.4891 mm, indicating a notable impact of this sub-region on monolayer formation. Gaps in D1a (G1a and G2a) present significantly lower mean values than CW measurements, underscoring considerable

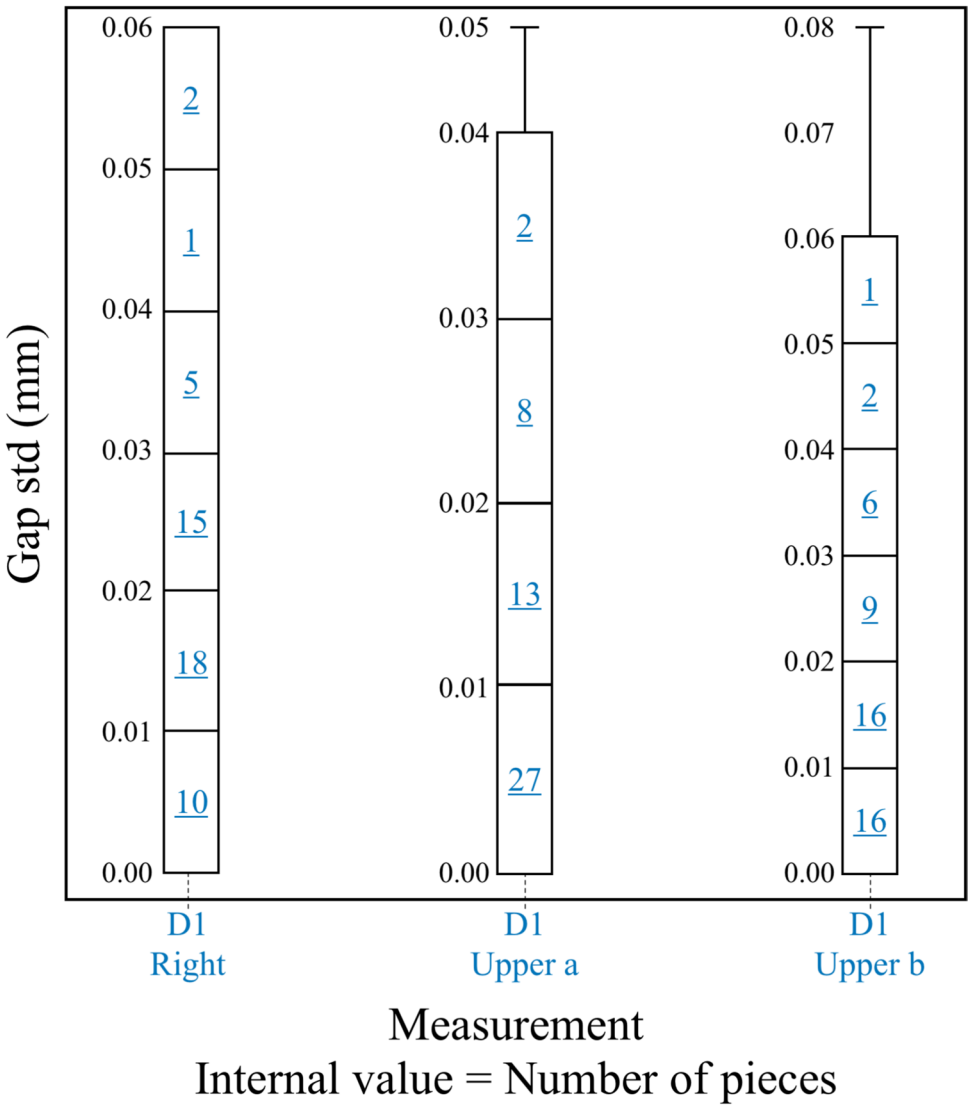

Fig. 14 Std gap between contours of each piece

Table 3 H-D1 Right region values

Condition	Monolayer feature	Value (mm)	
		Mean	Std
	CW1	0.6343	**0.0678**
H	CW2	0.5886	0.0392
	CW3	0.6043	0.0361
	CW1	0.4647	0.0232
	G1	0.1117	0.0162
D1	CW2	0.4402	0.0203
	G2	0.0958	0.0265
	CW3	0.5182	0.0295

differences likely due to specific process influences. All features in D1a exhibit standard deviations below the 0.05 mm threshold, highlighting precision within the acceptable tolerance.

Table 4 H-D1 Upper region values

Condition	Monolayer feature	Value (mm)	
		Mean	Std
	CW1	0.6474	**0.0784**
H	CW2	0.5890	0.0399
	CW3	0.5938	0.0433
	CW1a	0.4891	0.0230
	G1a	0.0921	0.0152
	CW2a	0.4463	0.0195
	G2a	0.0932	0.0218
	CW3a	0.5094	0.0314
D1	CW1b	0.3795	0.0311
	G1b	0.1884	0.0346
	CW2b	0.3451	0.0361
	G2b	0.1801	0.0469
	CW3b	0.4165	**0.0613**

Sub-region D1b shows further deviation with reduced mean widths (e.g., CW1b at 0.3795 mm) and gap measurements (G1b and G2b) that are higher than those in D1a. This points to a significant effect of sub-region D1b on monolayer feature formation. Standard deviations for D1b features, especially for gaps, exceed the tolerance threshold, indicating a higher degree of variability, possibly reflecting different material behaviors or process conditions specific to this sub-region.

In Table 5, which presents the H-D2 center region values, we analyze the monolayer features under conditions H and Defect 2 (D2), focusing on Raster Width Previous (RWP), Raster Width Center (RWC), Raster Width After (RWA), and the gap (G), with evaluations conducted on 50 workpieces for each condition.

In condition H, the mean values for RWP, RWC, and RWA demonstrate remarkable consistency, with a narrow range from 0.5315 mm to 0.5333 mm. This uniformity in raster width measurements indicates a stable and controlled process under condition H. However, the standard deviations for these features span from 0.0653 mm to 0.0872 mm, exceeding the printer's tolerance threshold of ± 0.05 mm. This indicates a variability beyond the expected precision, suggesting areas for process improvement, particularly in maintaining uniformity across the raster measurements.

Transitioning to the D2 condition, there's a noticeable adjustment in mean values, particularly with RWA increasing to 0.6587 mm. This increase aligns with the expected impact of the D2 defect, which is anticipated to cause a significant expansion in raster width after the defect. Such an increase in RWA underlines the pronounced influence of the D2 condition on the monolayer's dimensional integrity, a critical insight for understanding and mitigating the impact of such defects. The gap measurement (G) under D2 is notably distinct at 0.3502 mm, highlighting a significant feature characteristic introduced by this condition. However, the standard deviations for D2, despite reflecting the complexity and variability introduced by the defect, do not align with the printer's stringent tolerance of ± 0.05 mm, pointing to increased variability that necessitates closer scrutiny and process optimization.

Table 6 provides an analysis of the "d" monolayer feature values, distinguishing the meanings of the "d" feature under conditions D1 and D2 due to their different contexts.

Under condition D1, "d" represents the length variation between the initial points of the D1 defect within the gaps G1 and G2. The measurements for D1 across the right and upper regions are as follows: in the right region, a mean value of 1.7348 mm with a standard deviation of 1.0365 mm is observed, indicating a notable degree of variation in the defect lengths within this region. In the upper region, the mean value is 0.7480 mm with a standard deviation of 0.7806 mm, suggesting less variation in defect lengths compared to the right region, but still reflecting significant inconsistency.

Table 5 H-D2 Center region values

Condition	Monolayer feature	Value (mm)	
		Mean	Std
H	RWP	0.5326	**0.0787**
	RWC	0.5315	**0.0872**
	RWA	0.5333	**0.0653**
D2	RWP	0.5680	**0.0731**
	G	0.3502	**0.0860**
	RWA	0.6587	**0.0730**

Table 6 "d" monolayer features values

Condition	Region	Value (mm)	
		Mean	Std
D1	Right	1.7348	**1.0365**
	Upper	0.7480	**0.7806**
D2	Center	20.1708	**2.4103**

For condition D2, "d" signifies the overall length spanning from the beginning to the end of the D2-impacted region. Here, a single measurement in the center region shows a mean value of 20.1708 mm with a standard deviation of 2.4103 mm. This significantly larger mean value compared to D1's measurements highlights the extensive impact of the D2 condition, illustrating a considerable extent of the affected area. The standard deviation indicates variability in the length of the D2-impacted region across different workpieces, yet the variability is relatively smaller when considering the extensive length covered by the defect.

Beyond the features that lie exactly at the perturbed line, changes observed in neighboring lines and gaps proved informative. Flow errors and retraction-related seams alter the local thermal field, so the effect is not confined to a single fabrication line. The spatial footprint that emerges in the adjacent raster and the nearby gap strengthens class separability between D1 and D2 and indicates how large a region should be considered for compensation during monitoring or parameter tuning. In practice, this 'neighborhood' context stabilizes the decision because it reduces the chance of acting on an outlier value measured on one isolated line (Fig. 15).

A comparative analysis of the proposed approach and the main image-based evaluation methods in the FFF additive manufacturing literature is presented in Table 7. As observed, previous studies have primarily focused on the characterization of voids and inter-layer bonding under different printing conditions. For instance, [29] provides a review of published works related to void types in FFF parts, offering a conceptual classification without experimental measurements. Experimental studies such as [30] and [31] assess the influence of varying nozzle temperatures

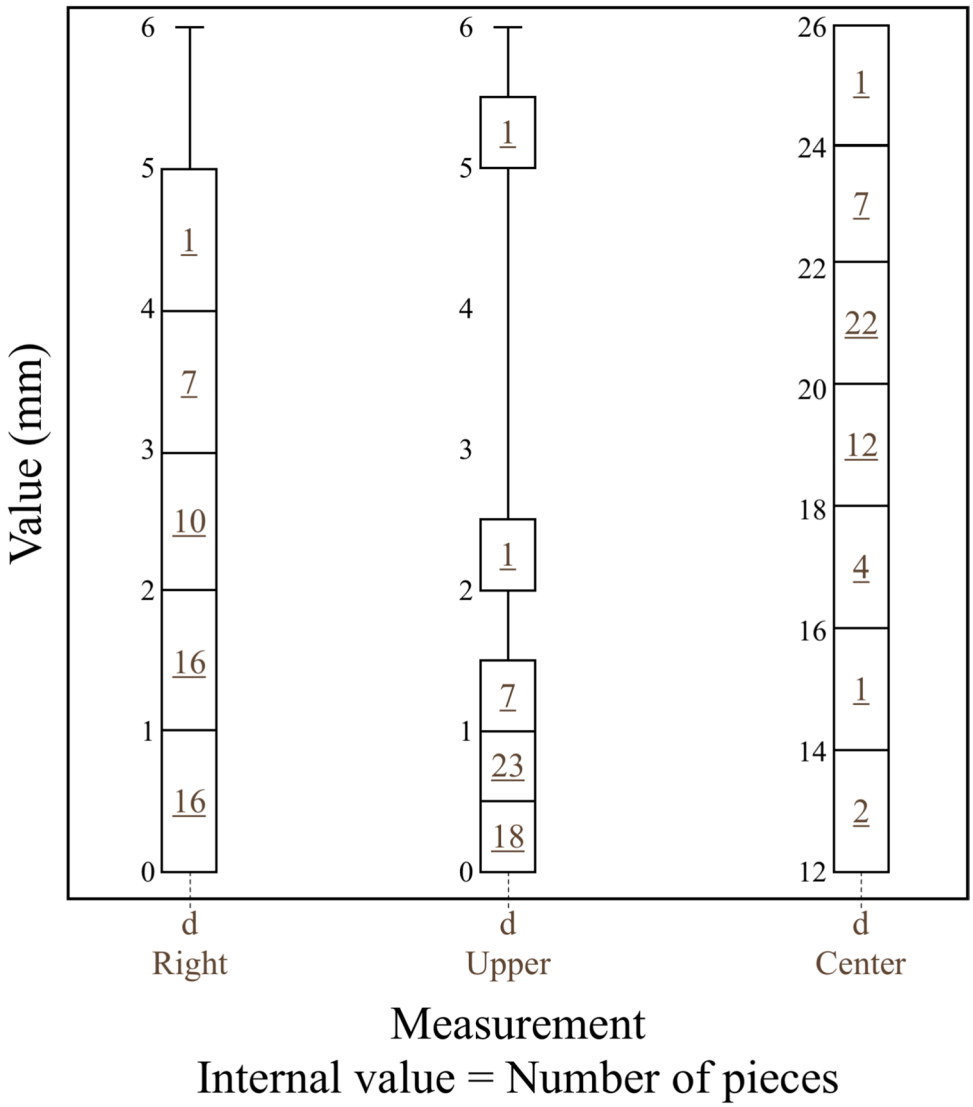

Fig. 15 "d" values of each piece

on void formation. While [30] applies optical microscopy on sanded cross-sections of PLA samples to evaluate void size, [31] uses scanning electron microscopy to analyze the morphology and distribution of voids in PEEK parts, emphasizing internal microstructural features.

Similarly, [32] investigates the effect of printing speed on inter-layer bonding by examining void sizes in meso-structures using optical microscopy, yet without a broader assessment of geometric consistency or surface-level deformations. Overall, these approaches tend to prioritize internal defects or bonding quality, with limited exploration of external surface characteristics or geometrical deviations caused by parameter variations.

In contrast, the present work focuses on the direct surface analysis of monolayer parts, combining contour and raster width distribution with gap measurements. Optical microscopy is employed not only for visualization but also for systematic quantification of surface features across different printing conditions. This integrated method enables a more complete characterization of geometric distortions at the layer level, offering valuable insights for process control and in-situ monitoring in FFF additive manufacturing.

4.3 Practical implications and envisioned applications

The distributions and comparative tables suggest immediate, first-layer acceptance windows that separate regular fabrications (H) from D1 and D2 signatures. For D2, the inter-raster gap in the central region clusters around 0.35 mm, and the 'raster-after' (RWA) width increases from ≈0.53 mm (H) to ≈0.66 mm (D2).

A practical screening rule for this printer-material setup is: flag a retraction-seam event when central-region $G \geq 0.30$ mm or $RWA \geq 0.60$ mm. For D1, contour widths on right/upper regions shift from ≈0.59–0.63 mm (H) to

Table 7 Comparative analysis

References	Proposed approach	Fundamental monolayer parameter evaluation method
[29]	A review of published papers related to the study of voids in the FFF printed parts	Assessment of different categories of voids
[30]	To evaluate the impact of varying nozzle temperatures on the inter-layer adhesion and void size	Optical microscopy of the sanded cross-sections of the printed PLA samples for the evaluation of void size
[31]	To evaluate the impact of varying nozzle temperatures on the voids amount	Scanning electron microscopy of printed PEEK parts micro-morphologies for the evaluation of the number and distribution of voids
[32]	To evaluate the impact of varying printing speed on the inter-layer bonding	Optical microscopy of printed coupons mesostructures to allow evaluation of void sizes
Present work	To evaluate the contour and raster width distributions and gap measurements of FFF monolayer parts under different printing conditions	Optical microscopy of the monolayer parts' surface, followed by systematic evaluation of the impact of the different conditions on the parts' surface features

≈0.44–0.49 mm, with cases as low as ≈0.38 mm; a practical rule is: flag under-extrusion if any first-layer contour width ≤ 0.50 mm in the affected region. These windows are not universal limits; rather, they are printer and material-specific starting points that can be recalibrated via a short setup run with a similar monolayer fabrication.

Two application paths follow directly. (i) Rule-based in-situ monitoring: a low-cost camera over the build plate extracts the same features; when thresholds are crossed, the machine pauses, or the slicer inflates flow and reduces retraction locally. (ii) ML labeling for broader deployment: our feature-and-label set (H vs. D1 vs. D2, by region) can train classifiers to identify defect class online, enabling closed-loop actions without manual inspection.

5 Conclusion

This study evaluated the geometric fidelity of monolayer FFF parts under regular conditions and two induced defects, D1 and D2. We analyzed contour and raster widths, inter-raster gaps, and the d feature across right, upper, and center regions. Regular printing stayed within printer tolerances, with right region contour widths between 0.5886 mm and 0.6343 mm and low variability. Under D1, widths and gaps were reduced with higher dispersion, for example, CW1 = 0.4647 mm and G1 = 0.1117 mm in the right region, and CW1b = 0.3795 mm and G1b = 0.1884 mm in the upper region. D2 produced the largest distortions in the center region, with d = 20.1708 mm on average and a standard deviation of 2.4103 mm, and increased raster after and raster prior widths from 0.5333 mm to 0.6587 mm and from 0.5326 mm to 0.5680 mm.

These patterns yield practical acceptance windows for first-layer screening and in-situ monitoring. For platforms similar to the GTMax3D A1V2 on PLA, flag D1 when any contour width in the affected region is ≤ 0.50 mm, and flag D2 when the central region gap is ≥ 0.30 mm or the raster after width is ≥ 0.60 mm. The same features can be extracted by a top-view camera and compared with calibrated limits to pause a build or apply localized flow or retraction adjustments. These limits also provide baseline labels for manufacturers and slicer developers during preset calibration and factory acceptance tests.

Considering neighboring lines and gaps improves robustness. Flow errors and retraction-related seams perturb the local thermal and pressure field, so the effect is not confined to a single trace. The spatial footprint that appears in the adjacent raster and the nearby gap strengthens class separability between D1 and D2 and indicates how large a region should be considered for compensation during monitoring or parameter tuning.

Although the focus was on the first layer because it offers the earliest visible decision point, the implications extend to subsequent layers. An increased gap or narrowed contour in the first layer reduces second layer overlap, which may weaken bonding and promote surface distortion. Next steps include testing propagation across stacked layers with D1 and D2, aligning image-based labels with time-stamped process signals, and running closed-loop trials where flow or retraction is adapted when thresholds are exceeded, aiming at more reliable and dimensionally accurate additive manufacturing.

Authors' contributions Lopes, Aguiar, and Conceição Junior planned the printing tests; Lopes, Monson, and Aguiar performed the printing tests; Lopes and Mattera performed the visual inspection of the pieces; Lopes, Monson, and Mattera wrote the paper; Aguiar and Conceição Junior supervised and reviewed the entire process.

Funding The Article Processing Charge (APC) for the publication of this research was funded by the Coordenação de Aperfeiçoamento de Pessoal de Nível Superior - Brasil (CAPES) (ROR identifier: 00x0ma614). This study was financed in part by the Coordenação de Aperfeiçoamento de Pessoal de Nível Superior—Brasil (CAPES), Code 001, through scholarship no. 88881.846265/2023–01 granted under the Programa de Doutorado Sanduíche no Exterior (PDSE), and through scholarship no. 88887.666942/2022–00; and by The National Council for Scientific and Technological Development (CNPq) under Grant #306774/2021–6 and Grant #445054/2024–7.

Data availability Not applicable.

Declarations

Ethics approval Not applicable.

Consent to participate All authors consent to participate in this paper.

Consent for publication All authors consent to the publication of this paper.

Conflicts of interest The authors declare no conflict of interest.

References

1. Cunico MWM, Cavalheiro JDM (2017) Analytical and experimental characterization of anisotropic mechanical behaviour of infill building strategies for fused deposition modelling objects. Proceedings of the 29th Annual international Solid Freeform Fabrication Symposium - An Additive Manufacturing Conference. https://hdl.handle.net/2152/89922
2. Farhan Khan M et al (2020) Real-time defect detection in 3D printing using machine learning. Mater Today Proc 42:521–528. https://doi.org/10.1016/j.matpr.2020.10.482
3. Srinivasan R, Nirmal Kumar K, Jenish Ibrahim A, Anandu KV, Gurudhevan R (2020) Impact of fused deposition process parameter (infill pattern) on the strength of PETG part. Mater Today Proc 27:1801–1805. https://doi.org/10.1016/j.matpr.2020.03.777
4. Solomon IJ, Sevvel P, Gunasekaran J (2021) A review on the various processing parameters in FDM. Mater Today Proc 37(xxxx):509–514. https://doi.org/10.1016/j.matpr.2020.05.484
5. Dey A, Yodo N (2019) A systematic survey of FDM process parameter optimization and their influence on part characteristics. J Manuf Mater Process. https://doi.org/10.3390/jmmp3030064
6. Kumar R, Ranjan N (2021) Influences of infill percentage, bed temperature and outer perimeters on elongation of 3D printed nylon 6. Mater Today Proc 48:1661–1665. https://doi.org/10.1016/j.matpr.2021.09.529
7. Ali MdH, Kurokawa S, Shehab E, Mukhtarkhanov M (2022) Development of a large-scale multi-extrusion FDM printer, and its challenges. Int J Lightweight Mater Manuf. https://doi.org/10.1016/j.ijlmm.2022.10.001
8. Wu H, Yu Z, Wang Y (2017) Real-time FDM machine condition monitoring and diagnosis based on acoustic emission and hidden semi-Markov model. Int J Adv Manuf Technol 90(5–8):2027–2036. https://doi.org/10.1007/s00170-016-9548-6
9. Straub J (2015) Initial work on the characterization of additive manufacturing (3D printing) using software image analysis. Machines 3(2):55–71. https://doi.org/10.3390/machines3020055
10. Wendt C, Fernández-Vidal SR, Gómez-Parra Á, Batista M, Marcos M (2016) Processing and quality evaluation of additive manufacturing monolayer specimens. Adv Mater Sci Eng 2016:1–8. https://doi.org/10.1155/2016/5780693
11. Fu Y, Downey A, Yuan L, Pratt A, Balogun Y (2021) In situ monitoring for fused filament fabrication process: a review. Addit Manuf 38:101749. https://doi.org/10.1016/j.addma.2020.101749
12. Wendt C, Valerga AP, Droste O, Batista M, Marcos M (2017) FEM based evaluation of fused layer modelling monolayers in tensile testing. Procedia Manuf 13:916–923. https://doi.org/10.1016/j.promfg.2017.09.160
13. Glissoi Lopes T, Marques Queiroz L, Bombonatti V, Carmo M, Aguiar P, França T (2021) The influence of printing parameters on monolayer part features in fused filament fabrication. In: Proceedings of the 26th international congress of mechanical engineering, Florianópolis/SC: ABCM. https://doi.org/10.26678/ABCM.COBEM2021.COB2021-0745
14. Volpato N (2017) *Manufatura Aditiva: tecnologias e aplicações da impressão 3D*, 1st ed. Blucher, São Paulo
15. Glissoi Lopes T, Carmo M, Marques Queiroz L, Aguiar P, França T (2021) Feasibility of optical profilometry for quality characterization of monolayer parts obtained by fused filament fabrication. In: Proceedings of the 26th international congress of mechanical engineering, Florianópolis/SC: ABCM. https://doi.org/10.26678/ABCM.COBEM2021.COB2021-0751
16. Lopes TG, Rocha IMM, Aguiar PR, França TV (2022) Influence of vibroacoustic phenomena from FFF process on surface characteristics of printed parts. Eng Proc 19(1):44. https://doi.org/10.3390/ECP2022-12615
17. Li Z, Zhang Z, Shi J, Wu D (2019) Prediction of surface roughness in extrusion-based additive manufacturing with machine learning. Robot Comput Integr Manuf 57:488–495. https://doi.org/10.1016/j.rcim.2019.01.004
18. do Carmo MGF, Lopes TG, Bombonatti VS, Aguiar PR, França TV (2020) Study of the defects and geometric anomalies on monolayer parts obtained by fused deposition modeling process. Proc West Mark Ed Assoc Conf 69(1):40. https://doi.org/10.3390/CGPM2020-07159
19. Liu J, Hu Y, Wu B, Wang Y (2018) An improved fault diagnosis approach for FDM process with acoustic emission. J Manuf Process 35:570–579. https://doi.org/10.1016/j.jmapro.2018.08.038
20. Fernandez-Vicente M, Calle W, Ferrandiz S, Conejero A (2016) Effect of infill parameters on tensile mechanical behavior in desktop 3D printing. 3D Print Addit Manuf 3(3):183–192. https://doi.org/10.1089/3dp.2015.0036
21. Gebisa AW, Lemu HG (2018) Investigating effects of Fused-deposition modeling (FDM) processing parameters on flexural properties of ULTEM 9085 using designed experiment. Materials 11(4). https://doi.org/10.3390/ma11040500
22. Es-Said OS, Foyos J, Noorani R, Mendelson M, Marloth R, Pregger BA (2000) Effect of layer orientation on mechanical properties of rapid prototyped samples. Mater Manuf Process 15(1):107–122. https://doi.org/10.1080/10426910008912976
23. Wu W, Geng P, Li G, Zhao D, Zhang H, Zhao J (2015) Influence of layer thickness and raster angle on the mechanical properties of 3D-printed PEEK and a comparative mechanical study between PEEK and ABS. Materials 8(9). https://doi.org/10.3390/ma8095271
24. Roschli A, Borish M, Feldhausen T, Barnes A, Wang P, MacDonald E (2024) The g-code file. In: Motion and path planning for additive manufacturing, Elsevier, pp 225–239. https://doi.org/10.1016/B978-0-443-15286-3.00002-3
25. Wu M, Phoha VV, Moon YB, Belman AK (2016) Detecting malicious defects in 3D printing process using machine learning and image classification. In: ASME international mechanical engineering congress and exposition, proceedings (IMECE). https://doi.org/10.1115/IMECE201667641
26. Lopes TG, Monson PMC, Aguiar PR, D'Addona DM, Júnior POC (2025) MonolayerFFF: an image dataset of monolayerFFF

3D printed parts with different fabrication conditions. IEEE Access 13:155277–155284. https://doi.org/10.1109/ACCESS.2025.3603958
27. Glissoi Lopes T, Monson PMC, Aguiar PR, Daddona DM, Conceição Junior PO (2025) MonolayerFFF. Mendeley Data: v3. https://doi.org/10.17632/k66f2gbgb4.3
28. do Carmo MGF, Lopes TG, Bombonatti VS, Aguiar PR, França TV (2020) Studying the defects and geometric anomalies on monolayer parts obtained via the fused deposition modeling process. In: The first international conference on "Green" polymer materials 2020. MDPI, Basel, p 40. https://doi.org/10.3390/CGPM2020-07159
29. Tao Y et al (2021) A review on voids of 3D printed parts by fused filament fabrication. J Mater Res Technol 15:4860–4879. https://doi.org/10.1016/j.jmrt.2021.10.108
30. Spoerk M, Arbeiter F, Cajner H, Sapkota J, Holzer C (2017) Parametric optimization of intra- and inter-layer strengths in parts produced by extrusion-based additive manufacturing of poly(lactic acid). J Appl Polym Sci 134(41). https://doi.org/10.1002/app.45401
31. Wang P, Zou B, Xiao H, Ding S, Huang C (2019) Effects of printing parameters of fused deposition modeling on mechanical properties, surface quality, and microstructure of PEEK. J Mater Process Technol 271:62–74. https://doi.org/10.1016/j.jmatprotec.2019.03.016
32. Abbott AC, Tandon GP, Bradford RL, Koerner H, Baur JW (2018) Process-structure-property effects on ABS bond strength in fused filament fabrication. Addit Manuf 19:29–38. https://doi.org/10.1016/j.addma.2017.11.002